AD-A277 744

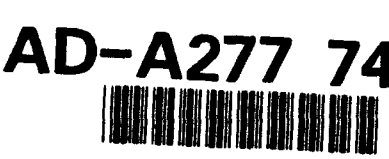

(2)

ARMY RESEARCH LABORATORY

Modeling the Impact Behavior of High Strength Ceramics

A. M. Rajendran

ARL-TR-224

December 1993

DTIC
ELECTE
APR 0 5 1994
S E D

94-10194

DTIC QUALITY INSPECTED 3

Approved for public release; distribution unlimited.

94 4 4 104

The findings in this report are not to be construed as an official Department of the Army position unless so designated by other authorized documents.

Citation of manufacturer's or trade names does not constitute an official endorsement or approval of the use thereof.

Destroy this report when it is no longer needed. Do not return it to the originator.

REPORT DOCUMENTATION PAGE

Form Approved
OMB No. 0704-0188

Public reporting burden for this collection of information is estimated to average 1 hour per response, including the time for reviewing instructions, searching existing data sources, gathering and maintaining the data needed, and completing and reviewing the collection of information. Send comments regarding this burden estimate or any other aspect of this collection of information, including suggestions for reducing this burden, to Washington Headquarters Services, Directorate for Information Operations and Reports, 1215 Jefferson Davis Highway, Suite 1204, Arlington, VA 22202-4302, and to the Office of Management and Budget, Paperwork Reduction Project (0704-0188), Washington, DC 20503.

1. AGENCY USE ONLY (Leave blank)	2. REPORT DATE	3. REPORT TYPE AND DATES COVERED
	December 1993	Final Report

4. TITLE AND SUBTITLE
Modeling the Impact Behavior of High Strength Ceramics

5. FUNDING NUMBERS

6. AUTHOR(S)
A. M. Rajendran

7. PERFORMING ORGANIZATION NAME(S) AND ADDRESS(ES)
U.S. Army Research Laboratory
Watertown, MA 02172-0001
ATTN: AMSRL-MA-PD

8. PERFORMING ORGANIZATION REPORT NUMBER
ARL-TR-224

9. SPONSORING/MONITORING AGENCY NAME(S) AND ADDRESS(ES)
U.S. Army Research Laboratory
2800 Powder Mill Road
Adelphi, MD 20783-1197

10. SPONSORING/MONITORING AGENCY REPORT NUMBER

11. SUPPLEMENTARY NOTES

12a. DISTRIBUTION/AVAILABILITY STATEMENT
Approved for public release; distribution unlimited.

12b. DISTRIBUTION CODE

13. ABSTRACT (Maximum 200 words)

An advanced constitutive model is used to describe the shock and high strain rate behaviors of silicon carbide (SC), boron carbide B_4C, and titanium diboride (TiB_2) under impact loading conditions. The model's governing equations utilize a set of microphysically-based constitutive relationships to model the deformation and damage processes in a ceramic. The total strain is decomposed into elastic, plastic, and microcracking components. The plastic strain component was calculated using conventional viscoplastic equations. The strain components due to microcracking utilized relationships derived for a penny-shaped crack containing elastic solids. The main features of the model include degradation of strength and stiffness under both compressive and tensile loading conditions. When loaded above the Hugoniot elastic limit (HEL), the strength is limited by the strain rate dependent strength equation. However, below the HEL, the strength variation with respect to strain rate and pressure is modeled through microcracking relationships assuming no plastic flow. The ceramic model parameters were determined using a set of VISAR data from the plate impact experiments.

14. SUBJECT TERMS	15. NUMBER OF PAGES
Impact, Ceramics, Modeling, Plate impact, High strain rate, Cracks	40
	16. PRICE CODE

17. SECURITY CLASSIFICATION OF REPORT	18. SECURITY CLASSIFICATION OF THIS PAGE	19. SECURITY CLASSIFICATION OF ABSTRACT	20. LIMITATION OF ABSTRACT
Unclassified	Unclassified	Unclassified	UL

DTIC QUALITY INSPECTED 3

Contents

Accesion For
NTIS CRA&I
DTIC TAB
Unannounced
Justification
By
Distribution /
Availability Codes
Dist | Avail and / or Special
A-1

List of Figures

List of Tables

Introduction

Ceramic materials are increasingly being used as armor elements, engine turbine blades, and other structural elements because of their enhanced dynamic compressive strength and high temperature properties. Understanding of ceramic behavior under impact loading conditions is essential in the design of improved impact resistant materials for dynamic structural and armor applications. For this purpose, a few impact/shock wave propagation experimental techniques are available. The experimental data are often used in the development of constitutive/damage models to describe the complex impact behavior of ceramic materials. An increasing use of advanced finite element/difference computer codes in the armor/anti-armor design analyses requires development of dependable and realistic material models in the codes. This requirement is all the more important for advanced materials such as the ceramics and glass fiber-reinforced plastic materials.

Recently, Rajendran (1,2) presented internal state variable-based constitutive equations to describe the impact behavior of ceramic materials. The model constants for AD85 ceramic were determined using the data from a combination of impact experiments including the uniaxial strain-based plate impact experiment and the uniaxial stress-based split Hopkinson bar (SHB), as well as the rod-on-rod experiments (3,4). The ceramic constitutive model assumes the following:

- Pre-existing randomly distributed flaws in the ceramics
- Plastic flow in the ceramics when shocked about the HEL
- No plastic flow in tension
- Degradation of elastic moduli under both compression and tension
- Pulverization occurs under compressive loading when the accumulated crack density reaches a value of 0.75. The flaws are activated according to a generalized Griffith criterion

There are three constants that characterize the virgin ceramics: number of microflaws (N_0^*), initial size of the flaw (a_0), and dynamic coefficient of friction (μ). For damage evolution, the model has two constants: crack growth factor (n_1) and crack growth index (n_2). These two loading-state dependent constants take different values under tension and compression. For most ceramics, n_1 and n_2 were assumed to be equal to one under tensile crack growth. The mode I fracture toughness (K_{IC}) is determined through direct measurements or from handbooks. At present, representative values for the model parameters were determined based on the model's ability to reproduce the measured stress/velocity profiles.

This work describes the modeling of three armor ceramics: titanium diboride (TiB_2), silicon carbide (SiC), and boron carbide (B_4C). The experimental data of Kipp and Grady (5) were employed in the modeling efforts. Steinberg (6), Johnson and Holmquist (7), and Addessio and Johnson (8) also employed the Kipp and Grady data in their modeling efforts. Recently, Mandell and Henninger (9) evaluated the ceramic models of Steinberg and Johnson-Holmquist using the MESA code (10).

In the Description of the Model Section the salient features of the ceramic model given in References 1 and 2 are briefly described. The Results and Discussion Section shows capabilities of the model in reproducing the VISAR data from the plate impact experiments. The various features of the ceramic model are explored through a series of simulations in which the model constants were systematically varied. The damaged moduli expressions of Margolin (11) are provided in the Appendix.

Description of the Model

The ceramic model assumes the existence of flaws (microcracks) in the virgin material. Therefore, the model does not require any microcrack nucleation criterion. The existing flaws are activated (extended) when the stress state satisfies the generalized Griffith's criterion. The effect of crack interaction due to coalescence is neglected. When the accumulating crack density reached a critical value, the model assumes pulverization of the ceramic.

Constitutive Relationships

The ceramic model assumes strains due to:

- Elastic and dislocation-based plastic deformations
- Microcrack opening and sliding
- Pore collapsing

In this section, the stress-strain relationship for a microcracked material is briefly discussed. The total strain is decomposed into elastic (ε^{e}_{ij}) and plastic strains (ε^{p}_{ij}) as

$$\varepsilon_{ij} = \varepsilon^{e}_{ij} + \varepsilon^{p}_{ij} \tag{1}$$

where the elastic strain consists of the elastic strain of the intact matrix material and the strain due to crack opening/sliding. The plastic strains associated with pore collapsing are modeled using the equations derived by Rajendran, et al., (12) for porous ductile aggregate. Plastic flow and pore collapse are assumed to occur in the ceramic only when the applied pressure exceeds the pressure at the Hugoniot elastic limit.

The elastic stress-strain equations for the microcracked aggregate material are given by:

$$\sigma_{ij} = M_{ijkl} \; \varepsilon^{e}_{kl} \; . \tag{2}$$

The components of the stiffness tensor M following Margolin's work (11) are given in Appendix A. The total stress σ_{ij} is decomposed into deviatoric stress (S_{ij}) components and pressure (P):

$$\sigma_{ij} = S_{ij} + P\,\delta_{ij} \; . \tag{3}$$

The pressure is calculated through the Mie-Gruniesen equation-of-state which is given by:

$$P = \left[P_H (1 - 0.5 \Gamma \mu) + \Gamma \rho_o (I - I_o) \right] \tag{4}$$

where

$$P_H = K_\gamma (\beta_1 \eta + \beta_2 \eta^2 + \beta_3 \eta^3) . \tag{5}$$

K_γ is the ratio of microcracks-degraded bulk modulus and intact bulk modulus. This ratio reduces from 1 to 0 as the elastic properties degrade with microcracking.

$\eta \left(= \frac{\rho}{\rho_o} - 1 \right)$ is the elastic volume strain (ε_V) and β_1, β_2, and β_3 are the empirical parameters. G is the Mie-Gruneisen parameter, ρ_o is the material's initial density, Io is the initial value of internal energy, and I is the current internal energy.

The elastic deviatoric stress-strain relationship is given by:

$$S_{ij} = 2 G \, (e_{ij} - e_{ij}^{p}) \tag{6}$$

where e_{ij} are the total deviatoric strains and G is the degraded shear modulus. The intact bulk and shear moduli were corrected for porosity using the correction factors as suggested by Johnson (13). The initial porosity, f_o, is a material model constant. The porosity is assumed to decrease due to pore collapsing at pressures above the HEL.

When the estimated von-Mises stress ($\sqrt{3 J_2}$) exceeded the compressive strength (Y) measured from the plate impact experiments, plastic flow is assumed and the deviatoric stresses were determined by satisfying the von-Mises criterion ($Y = \sqrt{3 J_2}$). The strain rate dependent compressive strength was described by a simple relationship:

$$Y = C_1 \, (1 + C_3 \ln \dot{\varepsilon}) \tag{7}$$

where C_1 and C_3 are model constants and $\dot{\varepsilon}$ is the applied strain rate. The constant, C_1, is assumed to be equal to Y_{HEL} which is calculated using the formula:

$$C_1 = Y_{HEL} = \frac{\sigma_{HEL}}{\left(\frac{K}{2G} + 1 \right)} . \tag{8}$$

σ_{HEL} is the maximum amplitude of the elastic shock. The constant, C_3, is calibrated by matching the "plastic wave" portion of the stress or velocity profiles of conventional planar plate impact experiments.

Definition of Damage

In the ceramic model, microcrack damage is measured in terms of the dimensionless microcrack density γ which is defined as:

$$\gamma = N_0^* a^3 \quad . \tag{9}$$

N_0^* is the average number of microflaws per unit volume and **a** is the maximum microcrack size which is treated as an internal state variable. The initial values of these two parameters are material model constants. The microcrack is assumed to extend when the stress state satisfies the Griffith's criterion (14,15). The extension of microcracks causes stress relaxation.

The Griffith criterion (14), employed in the model, includes the fracture toughness K_{IC}, as well as a dynamic frictional coefficient μ as model parameters. Since N_0^* is assumed to be a constant in the model, the increase in γ is entirely due to increase in the crack size. Experimental measurements to determine the initial number of microflaws in a unit volume and the initial maximum size of the microcracks are very difficult and tedious. The values are usually guessed and calibrated based on the model's ability to reproduce the measured stress/velocity histories in plate impact experiments.

Damage Growth Model

The crack extension (damage evolution) law is derived from a fracture mechanics-based relationship (16) for a single crack propagation under dynamic loading conditions and the law is described by:

$$\dot{a} = n_1 C_R \left[1 - \left(\frac{G_c}{G_I} \right)^{n_2} \right] \quad \begin{matrix} G_I \le G_c , \dot{a} = 0 \\ G_I > G_c , \dot{a} > 0 \end{matrix} \tag{10}$$

where C_R is the Rayleigh wave speed, G_c is the critical strain energy release rate for microcrack growth, and G_I is the applied strain energy release rate. The n_1 is used to limit the microcrack growth rate. The crack growth index n_2 affects the crack growth rate when the ratio $\frac{G_c}{G_I}$ is less than 1, but close to 1. Different crack extension rates are assumed for tensile and compressive loading conditions and, therefore, n_1 and n_2 are different (n_1 is n_1^- and n_2 is n_2^- for crack sliding; n_1 is n_1^+ and n_2 is n_2^+ for crack opening, accordingly). The ceramic is assumed to pulverize under compression when γ reached a critical value of 0.75 as described in Reference 1. The strength of the post-fractured ceramic is described by:

$$Y = \alpha + \beta P \tag{11}$$

where α and β are the model constants. In the present work, values for these two post-fracture model constants are arbitrarily assumed to be equal to 0 and 1, respectively. In a later section, the effect of β on the stress computed profiles are presented to justify the assumption of one for β.

Plate Impact Experiment

Plate impact tests provide a loading path that is very different from conventional SHB tests. The deformation is that of one-dimensional strain, and the mean stress is generally very high compared to that in the SHB tests under one-dimensional stress state. Strain rates are 10^5/s or higher. The material undergoes compression followed by tension. In general, plate impact experiments are essential for calibrating and validating high strain rate material models that aspire to general applicability.

Figure 1 shows typical velocity profiles that correspond to different levels of spallation, including a case where spallation does not occur. The challenging part of modeling the impact behavior of ceramics is in the model's ability to reproduce these profiles at various velocity levels using the same set of model parameters. The various levels of spall occur according to the impact velocity levels for a given flyer-target configuration. The thickness and material of the flyer plate affects the pulse duration. Model constants were determined by matching the computed velocity profiles with experimentally measured profiles. By trial and error, the model constants are improved from the initial guess. A set of constants based on the best match between the simulated time histories of stress and/or velocity and the experimental data is the preliminary values for the constants. This set may not assure the generality of the model constants; however, a few constants can be further improved by calibrating them against data from some other experimental configurations. Rajendran and Grove (4) exercised this approach for AD85 ceramic and determined a set of constants that were configuration independent.

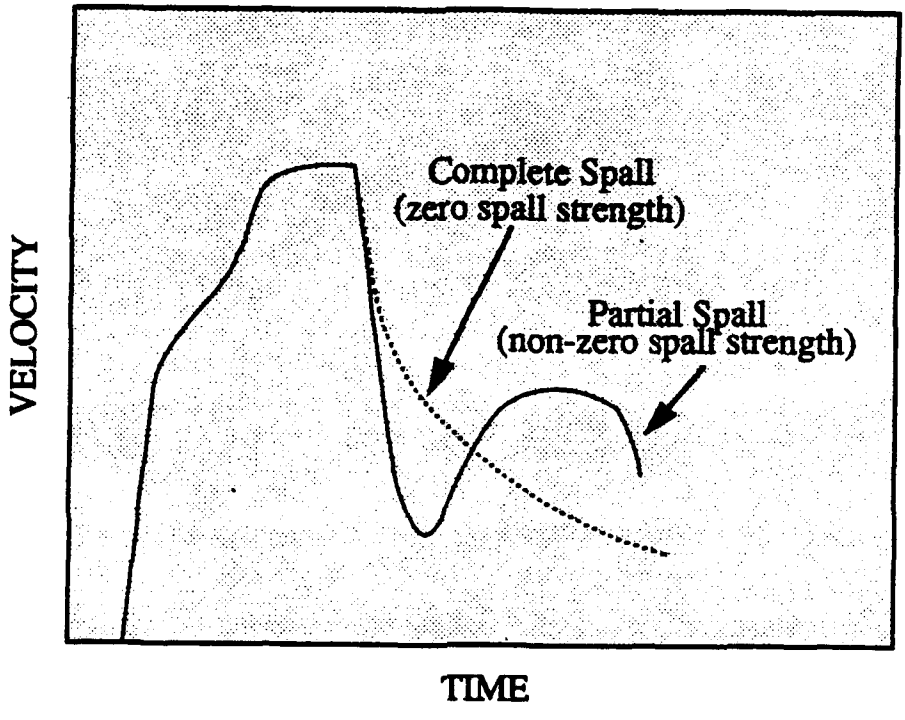

Figure 1. A sketch of typical velocity profiles indicating various levels of spalls.

The plate impact tests considered in the present study were conducted by Kipp and Grady (5) to determine:

- Hugoniot elastic limit
- Spall threshold of SiC, B_4C, and TiB_2
- Stress-strain path.

Kipp and Grady provide a detailed discussion on their plate impact experiments in Reference 5. The model parameters determination scheme fully utilized the plate impact test data of Kipp and Grady for SiC, B_4C, and TiB_2.

Results and Analyses

This section describes the shock response to the three ceramic materials based on the plate impact experimental simulations using the ceramic model presented in the previous section. In the simulation, the ceramic strength and stiffness were assumed to degrade due to microcracking. Recently, Grove (17) implemented the ceramic model into the 1991 version of the EPIC code (18). To determine the constants for SiC, B_4C, and TiB_2 using the VISAR data of Kipp and Grady (5), this version of the EPIC code was employed. The dimensions of the flyer and target plates, as well as the impact velocities in the plate impact experiments of Kipp and Grady, are given in Table 1. The shock stresses (maximum axial stress) in these experiments were two to four times the Hugoniot elastic limit of the ceramics. The window material was lithium fluoride whose density was 2641 kg/m^3.

Table 1. Kipp and Grady (5) plate impact experimental details

Test no.	Material	Impact velocity (m/s)	Flyer thickness (mm)	Target thickness (mm)
1	SiC	1542	3.987	8.939
2	SiC	2100	3.995	8.940
3	B_4C	1546	3.920	9.044
4	B_4C	2210	3.917	9.033
5	TiB_2	1515	3.972	10.804
6	TiB_2	2113	3.337	10.747

Kipp and Grady performed plate impact experiments at two velocities for each of the three ceramics; one at a lower level of about 1.5 km/s, and the other at a higher level of about 2.1 to 2.2 km/s. The ceramic model constants were determined using the lower velocity experiments. In other words, only tests 1, 3, and 5 were employed in the model constants calibration scheme. Later, the VISAR results of the higher velocity tests 2, 4, and 6 were predicted through EPIC simulations by employing the values determined from the low velocity tests.

Mesh and Time Step Sensitivity Study

Since the governing constitutive equations are coupled, nonlinear equations, a stable and accurate solution demands a robust numerical scheme which will assure not only convergence of the solution but also yield mesh and time step independent solutions. Grove (17) used a diagonally implicit Runge-Kutta scheme in the implementation of the model into the EPIC code. The simulations utilized the one-dimensional strain option in the EPIC code to model the plate impact configuration. To investigate the effect of time step and mesh size on the numerical results, two different time steps and meshes were respectively considered. A base line profile for a 0.2 mm mesh was obtained from a plate impact simulation. The model parameters used in the base line profile are $N_0^* = 10^9$; $a_o = 0.005\,mm$; $K_{IC} = 4\,MPa\sqrt{m}$; $\mu = 0.1$; $n_1^- = 0.1$. In the sensitivity study, the effect of mesh, time step, and the model parameters on the simulated velocity profile is compared with this base line profile.

To investigate the mesh-size effect, simulation with a 0.1 mm mesh (fine mesh) was performed and the corresponding velocity profile is compared with the base line profile (solid line) in Figure 2. The results were almost identical, as can be seen from Figure 2. The kink at the HEL in fine mesh was more pronounced than the corresponding kink in the coarse mesh. The time step effects were studied using two time steps; one with a maximum allowable time step of 0.01 ms and two with 0.001 ms. The velocity time histories from these two simulations were almost identical, as can be seen from Figure 3, confirming minimum influence of the time step on the numerical results.

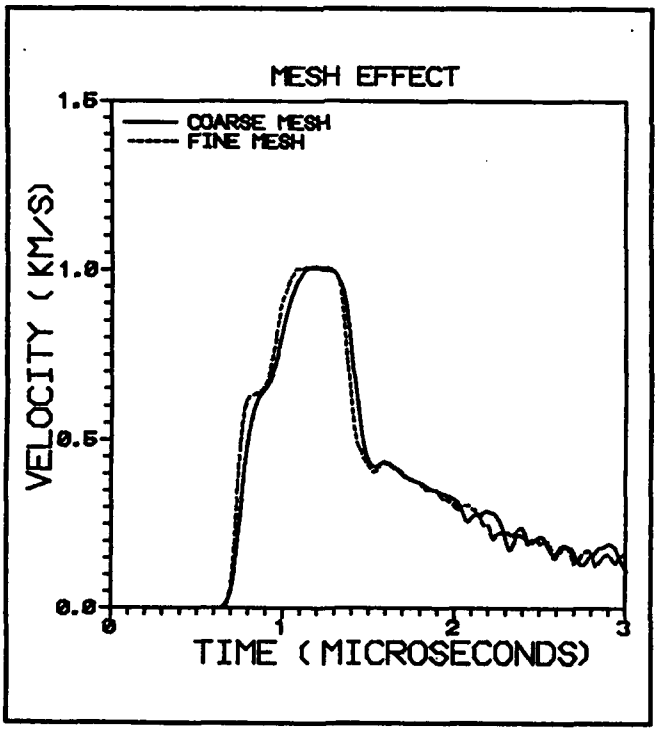

Figure 2. The effect of mesh size on the computed velocity profile.

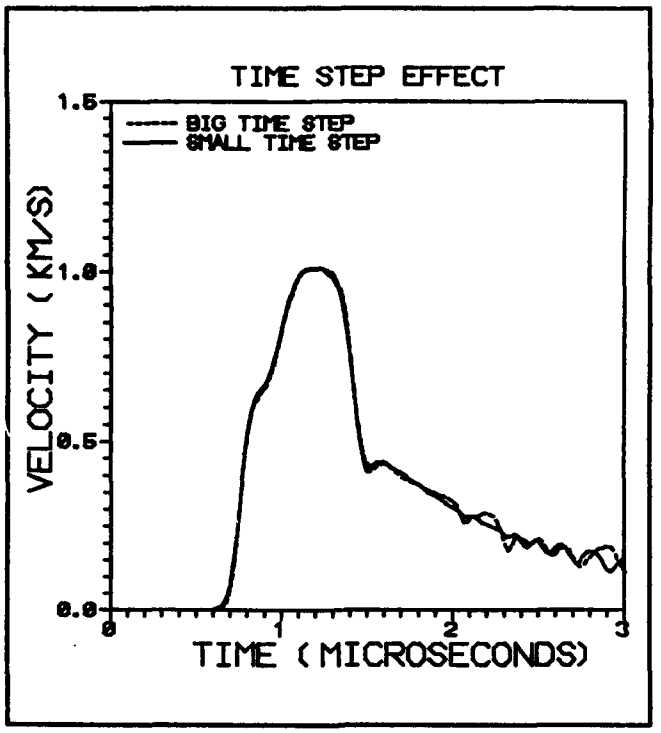

Figure 3. The effect of time step on the computed velocity profile.

Sensitivity Study on Model Constants

There are eight constants in the ceramic model to describe the microcracking behavior: N_0^*, a_o, μ, n_1^-, n_2^-, n_1^+, n_2^+, K_{ic}. For tensile loading (negative pressure), the crack growth factor n_1^+ and the crack growth index n_2^+ are assumed to be equal to one. Under compressive loading (positive pressure), the best suitable values for n_1^- and n_1^- are determined by matching the computed profile with the plate impact experimental data. To understand the significance of several of the model constants on the shape and amplitude of the measured velocity histories, a sensitivity study was carried out in the present work. Direct measurements of the microcrack parameters a_o, N_0^*, and μ (dynamic coefficient of friction) are extremely difficult. The estimation of realistic values for these constants requires microstructural characterization of the virgin ceramic through both nondestructive and destructive test techniques.

In the present modeling efforts, due to a lack of experimental measurements, the initial microcrack size is assumed to be equal to a fraction of average grain size; therefore, the number of flaws is determined through numerical simulations of the plate impact experiments. In effect, there are only four adjustable constants to describe the microcracking behavior: N_0^*, a_o, μ, and n_1^-. Therefore, the main idea behind the sensitivity study is to identify a range of values for these four model parameters and isolate the effect of any one parameter, or a combination of parameters, on certain portions of the stress/velocity history. Based on the sensitivity analyses, it may then be possible to develop a standard methodology to estimate appropriate values for the model constants.

Number of Flaws, N_0^*

Three simulations were considered using the values of 10^{11}, 10^9 (base line case), and 10^7 for N_0^*. The corresponding results are presented in Figure 4. A value of 10^7 did not produce complete spall fracture. The ceramic retained some of its spall strength, as one can see from the dashed line curve beyond point "S". The intermediate value 10^9 caused partial compressive cracking followed by tensile cracking. When the compressive microcracking is absent for $N_0^* = 10^9$, the pulse duration is according to the intact ceramic properties. In this case, the microcracking of the ceramic begins during unloading and spalls the ceramic completely, as indicated by the profile between points "D" and "E" of the solid curve. Based on these simulations, a value of 10^9 seems to be a possible value for N_0^* in order to cause spall without excessive compressive damage. A high value of 10^{11} caused excessive damage under compression and complete spall occurred. The velocity profile between point "A" and point "C" significantly differs from the results for 10^9 and 10^7; this can be explained by analyzing the pressure, damage, and axial stress histories inside the target.

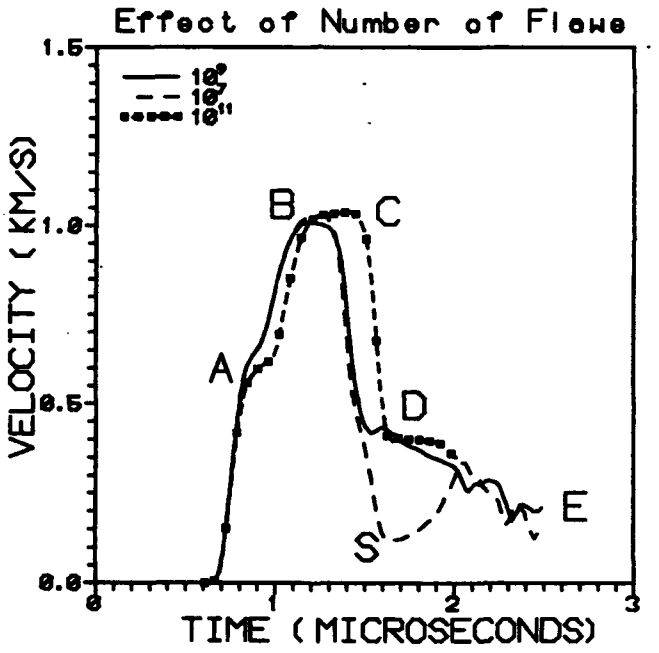

Figure 4. The effect of the number of flaws on the computed velocity profile.

For this purpose, an element very close to the impact plane is considered and the time histories of these three quantities are plotted in Figure 5. The pressure and stress are normalized with respect to σ_{HEL} so that the damage history can be presented in the same plot. A value of 15 GPa was used in the normalization. The microcracking behind the shock wave under compressive pressure (the code treats the compressive pressure as a positive quantity) causes damage in the ceramic. The damage reaches one at about 0.25 μs.

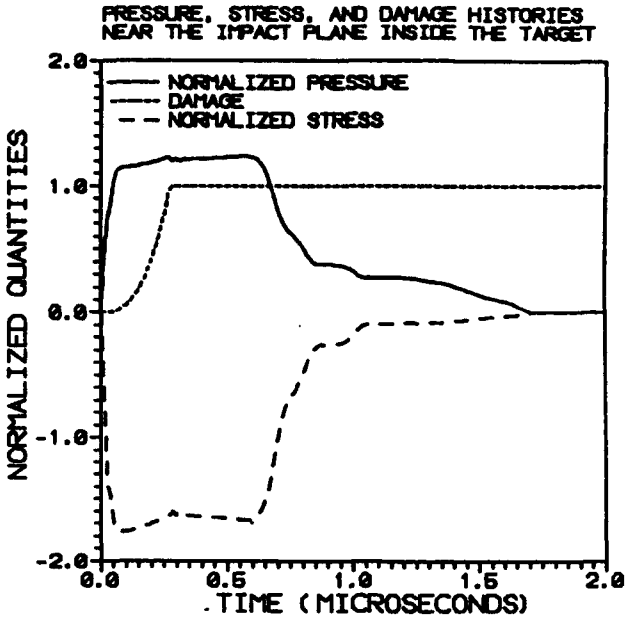

Figure 5. The time histories of pressure, stress, and damage in an element near the impact plane

Upon high velocity impact loading conditions, the ceramic material pulverizes under compressive pressure. In Figure 5, pulverization occurs at about 3 μs. The normalized pressure level continues to remain at the same level beyond the point of pulverization. Since the bulk modulus does not degrade under compressive pressure according to the model, especially when the three principal stresses are compressive, the shock pressure level did not change.

Due to absence of dilatation under high confinement pressure, the density of the confined granular ceramic remains the same as that of the intact ceramic. When one of the three principal stresses becomes tensile while the pressure remains under compression, crack opening could occur causing dilatation. Under such loading conditions the bulk modulus will degrade in the modeling. This is not the case for an element that is close to the impact plane, as can be seen from the normalized (principal) stress plot (see the dashed line in Figure 5). This axial stress remains compressive eliminating any bulk modulus degradation possibilities.

Initial Microcrack Size, a_o

To investigate the effect of microcrack size on ceramic fracture, three simulations with values 0.1 micron (μm), 0.2 μm, and 0.5 μm for a_o were considered. In these simulations, μ was 0.1 and N_0^* was 10^9. The velocity time histories for the three values are plotted in Figure 6. A small flaw size of 0.1 μm and below did not cause any microcracking.

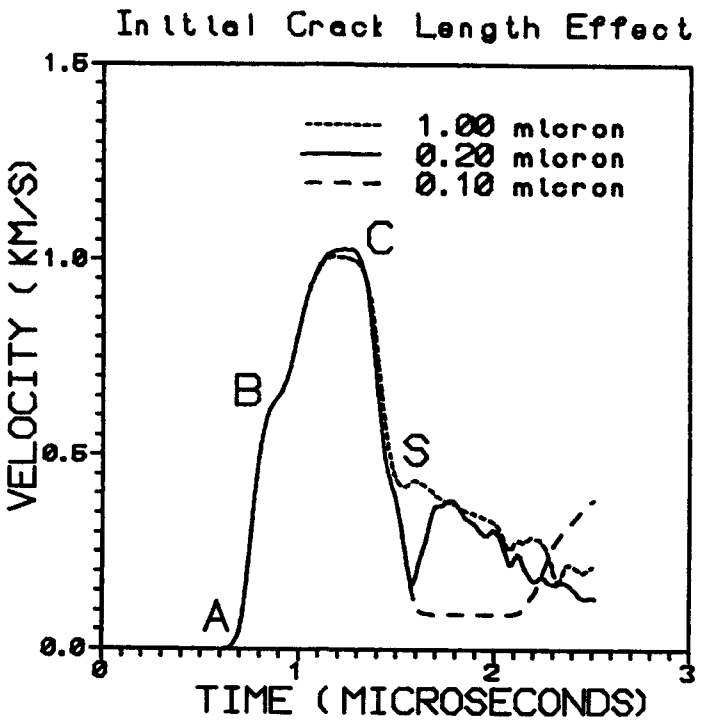

Figure 6. The effect of initial crack size on the computed velocity profile.

An additional simulation with $a_o = 0$ reproduced the result of the 0.1 μm crack. The 0.2 μm flaw caused partial spall. The crack sizes greater than 0.35 μm induced complete spall in the target. A microcrack size between the range of 0 to 0.35 did not influence the loading wave portion of the profile between points "A" and "C" as well as the elastic release between points "C" and "S". The range will vary according to different values of the other two microcrack parameters, μ and N_0^*.

Coefficient of Friction, μ

Figure 7 shows the effects of μ on the velocity profile for $n_1^- = 0.2$. The main influence of this parameter is to decrease the effective shear stress (τ - μP) level to satisfy the Giffith criterion under compressive pressure. τ is the applied shear stress and P is the pressure on the crack surface. Several simulations were performed to investigate this influence. The results indicated that the role of this parameter was closely tied to the values chosen for the other microcrack constants, especially the compressive crack growth factor n_1^-. For instance, the effect of μ was insignificant for $n_1^- = 0.1$; whereas, the effect became significant for $n_1^- = 0.2$.

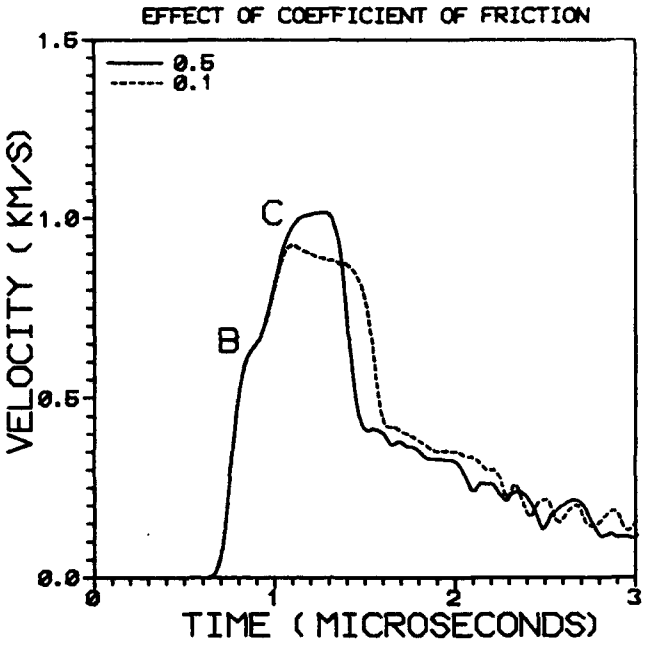

Figure 7. The effect of coefficient of friction on the computed velocity profile.

The lower values caused premature microcracking while the shock amplitude was still increasing during the "plastic" wave ramp between points "B" and "C". Since the compressive microcracking occurred well above the threshold level of "complete spall (under tension)," the influence of μ on the spall signal was negligible. This study suggests that a minimum value which will not cause any premature compressive damage shall be assigned to μ. In fact, this minimum value will allow the independent determination of other constants. In the modeling, a value of 0.1 was assumed for μ for SiC, B_4C, and TiB_2.

Compressive Crack Growth Factor, n_1^-

This constant limits the damage growth rate (see Equation 10) under compression to $n_1 C_R$. When the Griffith criterion is satisfied for a given stress state, the time dependent microcrack extension controlled the rate at which the elastic moduli are degraded. This degradation affects the shock wave speed and this, in turn, affects the pulse duration. Experimentally measured values are available for the limiting dynamic crack propagation velocity under the crack opening mode. However, such measurements are not available for dynamic crack propagation under mode II (crack sliding under shear). The n_1^- effect on the computed velocity profile is shown in Figure 8.

A value that is lower than 0.1 did not introduce any further change in the profile. The increasing values between 0.1 and 0.2 widened the pulse width due to elastic moduli degradation. The shock amplitude diminished as the microcracking increased with increasing n_1. The spall rebound portion of the velocity profile was not significantly affected when n_1^- was varied in the simulations. This is because the degradation of the elastic properties during compression is well above the threshold to cause complete spall upon the arrival of tensile stress wave.

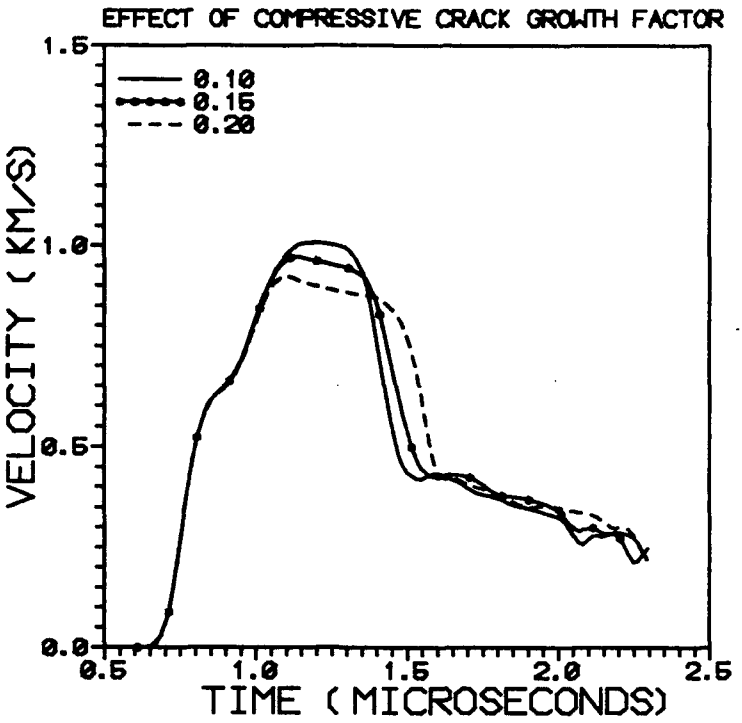

Figure 8. The effect of compressive crack growth factor on the calculated velocity profile.

Compressive Crack Growth Index, n_2^-

To verify the effect of n_2^- on the velocity profile, several simulations were performed. The results showed that the computed profile was unaffected by n_2^-. Since the ratio between G_c and G_I is large at impact velocities above 1 km/s, the values of this index between 0.001 and 1 did not alter the ceramic response. However, two additional simulations at a lower velocity also produced very similar wave profiles. In these simulations the initial microcrack size was assumed to be equal to 1 μm. Grove, et al., (3) found that this index influenced the computed stress histories in a ceramic rod due to an impact by a similar, but shorter rod at low velocity. In their study, the states of stress and strain at the gauge location were one-dimensional (uniaxial) stress and three-dimensional strain, respectively, whereas in the plate impact configuration, the stress state was three-dimensional and the strain state was one-dimensional.

Tensile Crack Growth Factor n_1^+

Ceramics are weak under tensile loading. The fracture toughness of a ceramic is very low compared to metals. Upon high velocity impact, the compressive shock loading causes damage in the ceramics. When the tensile wave arrives at locations where the ceramic has been partially damaged due to the initial compressive shock, it induces additional damage leading to complete spall. The computed velocity profiles for n_1^+ equal to 0.2, 0.3, and 1.0 are shown in Figure 9.

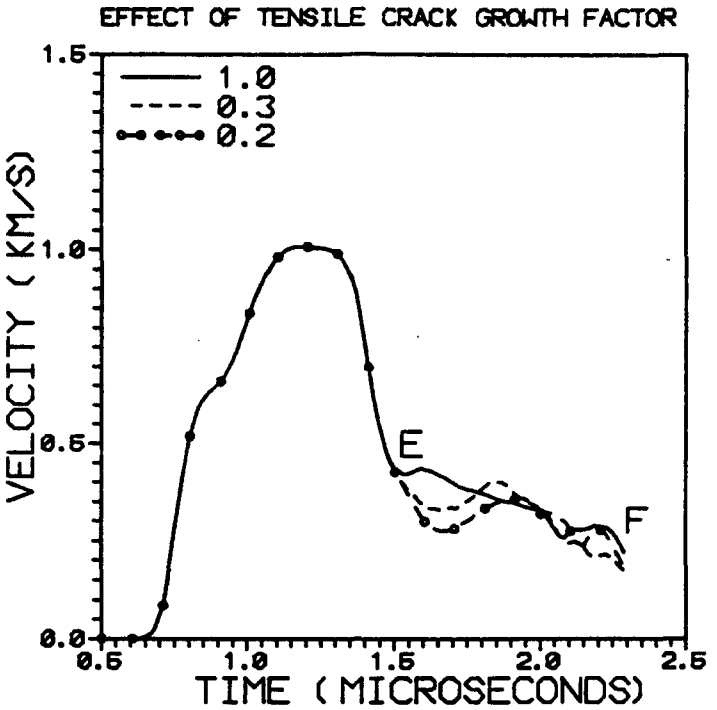

Figure 9. The effect of tensile crack growth factor on the computed velocity profile.

The crack density levels increase with an increasing value of n_1^+. Since the degradation of spall strength is not complete for lower values of n_1^+, the calculated profiles showed pullback signals (spall rebounds) indicating nonzero spall strength. The value of 1 caused complete spall in the ceramic target, as can be seen from the velocity profile between points "E" and "F" (solid curve). By comparing these simulations with an experimental profile, a suitable value for tensile n_1 can be chosen while modeling the impact behavior of any ceramic. Experimental measurements on a single crack propagation under dynamic loading conditions suggest that the Rayleigh's wave speed is the limiting value for this factor; therefore, in the present analysis a value of 1 was used for all three ceramics eliminating the need for determining the constants from the plate impact experiments.

Tensile Crack Growth Index, n_2^+

This parameter appears in the damage evolution law of Equation 10 as n_2. The ratio of critical strain energy release rate (with respect to crack extension), G_c, and applied strain energy release rate, G_I, is modified through n_2. The ratio is equal to 1 when $G_c = G_I$. The crack growth occurs when the ratio is below 1. As soon as the Griffith criterion is satisfied and when the ratio is closer to 1, this index influences the microcracking rate. However, the effect on the computed velocity profile is significant only for extremely low values of the index as shown in Figure 10.

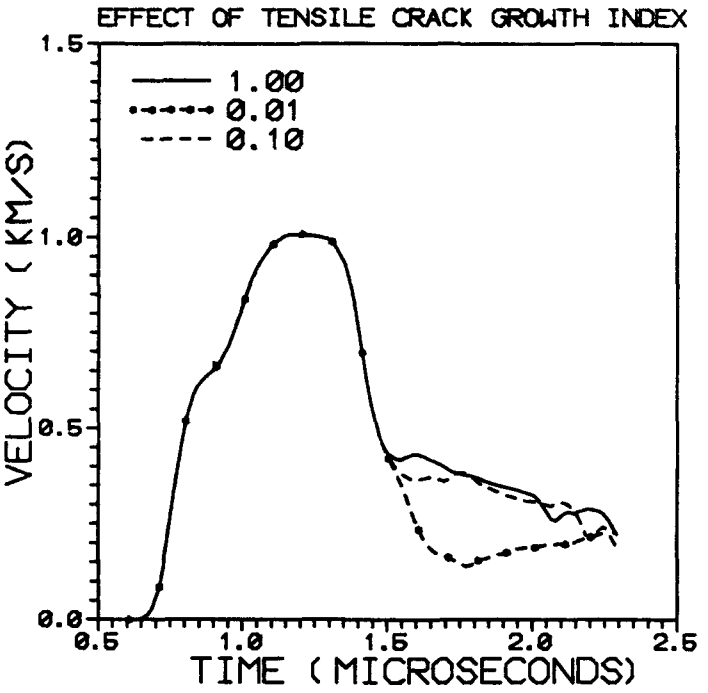

Figure 10. The effect of tensile crack growth index on the computed velocity profile.

A value of 0.01 suppressed the spall fracture, though the Griffith criterion was satisfied. The larger values 0.1 and 1.0 produced complete spall and the corresponding profiles were similar; therefore, to cause complete spall, a value between 0.1 and 1 can be chosen for the tensile crack growth index n_2. For simplicity, a value of 1 is chosen for the three ceramics.

Fracture Toughness, K_{IC}

The ceramic model does not contain any microflaws nucleation model. A number of flaws are assumed to exist in the virgin ceramic materials. These flaws are activated when the stress state satisfies the Griffith criterion for an initial maximum flaw of size, a_0. The value of K_{IC} between 1 $MPa\sqrt{m}$ and 20 $MPa\sqrt{m}$ did not show any effect on the velocity history. In the modeling, the static fracture toughness values from handbooks were used for the three ceramics.

Post Fracture Strength Parameter β

The plate impact experimental configuration seems to be insensitive to this parameter. The simulations with three different values for β showed hardly any effect on the computed velocities profiles, as can be seen from Figure 11. In the post-fracture-strength Equation 11, the strength of the pulverized ceramic is directly proportional to the applied pressure when $\alpha = 0$. The strength is zero for $\beta = 0$; twice the pressure for $\beta = 2$, and equal to the pressure for $\beta = 1$.

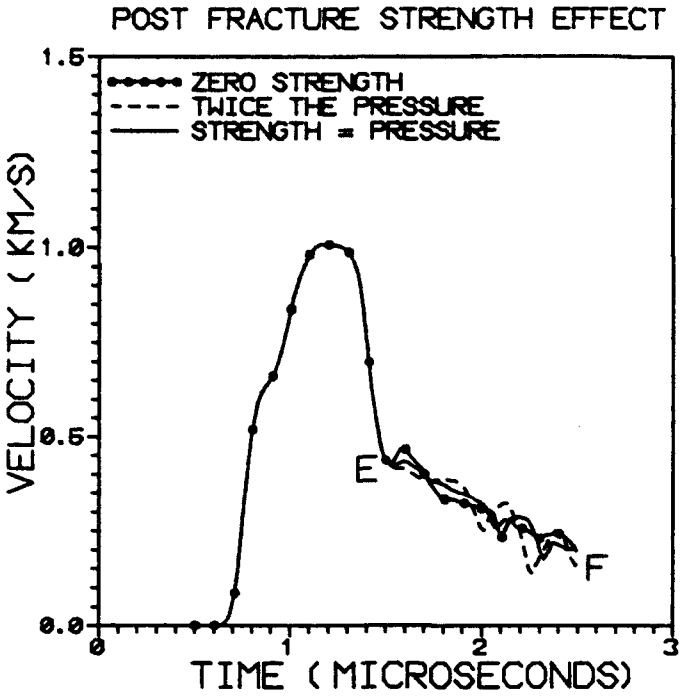

Figure 11. The effect of post-fracture strength model parameter β on the computed velocity profile.

The average spall signal between points "E" and "F" is almost the same for these three values. It appears that the calibration of this parameter should be based on some other type of impact test configurations such as the configuration in which a rod penetrates into a ceramic plate. The computed stress profiles for three values of α = 1, 5, and 10 kbars did not influence the results either; therefore, in the model constant calibration scheme, α was set to zero for three ceramics.

Silicon Carbide (SiC)

The shock portion of the wave profile for SiC resembled a typical wave profile of a rate sensitive metal. In fact, Kipp and Grady (5) successfully modeled the low and high velocity tests on SiC using a strain hardening model applicable for metals. The absence of large release wave dispersion in SiC enabled the successful use of a simple metal-based model. The experimental data did not reveal any phase transformation in SiC up to about 36 GPa. The HEL kink appears at about 15 GPa in both tests.

A set of best suitable values for the constants were determined by matching the model generated velocity profile with the experimental data of test 1 (see Table 1). The corresponding values are given in Table 2. The equation-of-state parameters β_1, β_2, β_3, and Γ are given in Table 3. These values were employed by Johnson and Holmquist (7) in their modeling of Kipp and Grady's experimental data.

Table 2. The ceramic model constants

Model constants	B_4C	SiC	TiB_2
f_o (porosity content)	0.03	0.0	0.0
K_{IC} (MPa $\sqrt{m}$) (fracture toughness)	2	4	7
μ (coefficient of friction)	0.1	0.1	0.1
N_0^* (m^{-3}) (number of flaws)	$5x10^9$	$1x10^9$	$1x10^9$
n_1	0.1	0.1	0.15
a_o (microns) (initial crack size)	0.5	0.5	2.0

Table 3. Equation-of-state and strength constants

Other constants	B_4C	SiC	TiB_2
Density (kg/m3)	2516	3177	4452
β_1 (GPa)	233	204	230
β_2 (GPa)	50	204	930
β_3 (GPa)	0	0	-1310
Γ	1	1	1
Y_{HEL} (GPa)	12.5	11.5	12.0
C_3	0.01	0.01	0.01
G (GPa)	199	187	237

Figure 12 compares the ceramic model generated velocity versus time plot with the Kipp and Grady data for SiC at an impact velocity of 1542 m/s. The model reproduced all the salient features of the data. As the next step, the high-stress experiment (see test 2 in Table 1) at an impact velocity of 2100 m/s was simulated using the same set of values for the model constants. The simulation predicted velocity profile matched the data extremely well, as shown in Figure 13. The ceramic model reproduced all the salient features of the experimental data.

The simulated stress-strain path in the center of the SiC target is plotted in Figure 14. In this figure, the compressive stress and compressive pressure are plotted as positive quantities. The computed HEL is about 18 GPa. The experimental value was about 15 GPa. The increased value in the computation is due to the strain rate dependent term in Equation 7. It is possible to lower the value of C_1 and adjust the value of C_3 to match the computed stress at HEL with the data. However, for the sake of simplicity in the model constant determination scheme, the value of Y that corresponds to the stress at HEL (see Equation 8) is assigned to C_1.

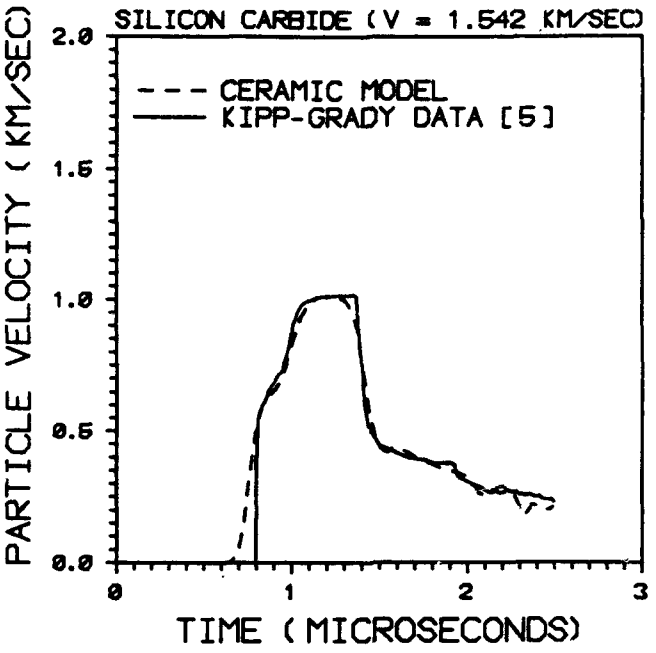

Figure 12. A comparison between model generated velocity profile with the Kipp and Grady plate impact experimental data at impact velocity 1542 m/s for silicon carbide.

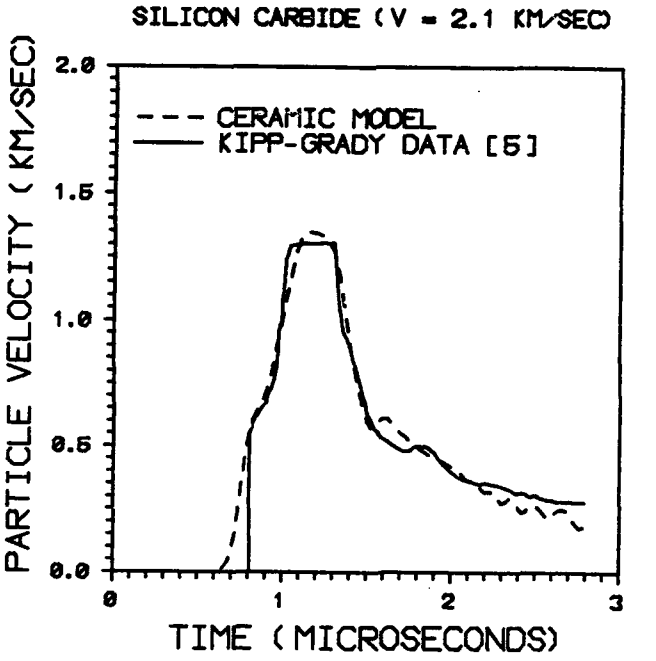

Figure 13. A comparison between model generated velocity profile with the Kipp and Grady plate impact experimental data at impact velocity 2100 m/s for silicon carbide.

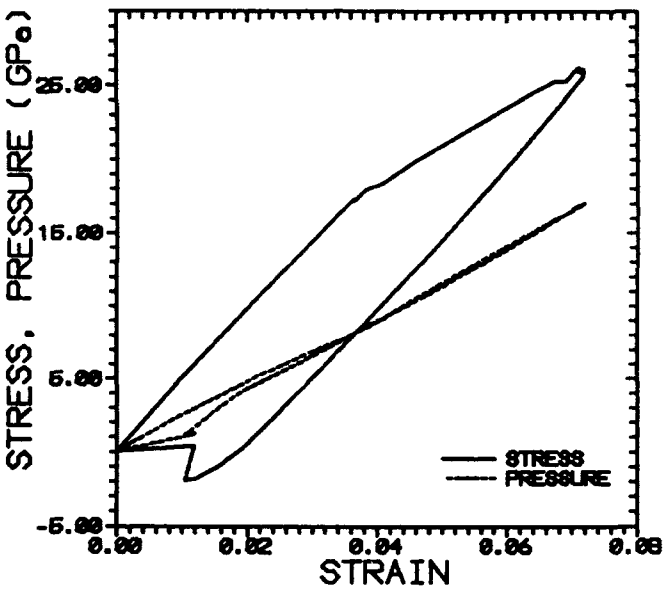

Figure 14. The stress-strain path (under one-dimensional strain) in the midplane of an SC target. The dotted line is the computed hydrostat.

Therefore, the transition from elastic to plastic deformation is controlled by the strain rate dependent strength. A value of 12.5 GPa was employed in the simulation. Though C_1 was chosen to be equal to this value, the high $\dot{\varepsilon}$ ($>10^4$/s) slightly increased the value of Y. This, in turn, caused a slight increase in the computed σ_{HEL}. Kipp and Grady obtained a value of about 16 GPa in their computational analysis. The maximum stress amplitude in compression reached about 26 GPa and elastically unloaded past the hydrostat (see the dotted line curve).

At about 0.02 strain, the stress became tensile and reached a tensile maximum of about 2 GPa. The ceramic model reduced the stress amplitude in tension due to microcracking. The ability to control the tensile stress amplitude is an important feature of the model. The degradation of the tensile strength due to microcracking was a continuous process (not an instantaneous process) and, therefore, the stress relaxation occurred continually until the microcrack density reached a critical value of 9/16, according to the Budiansky and O'Connell solution (19) for tensile pressure loading conditions.

Johnson and Holmquist (7), Steinberg (6), and Addessio and Johnson (8) successfully reproduced the measured velocity profiles of Kipp and Grady (5). In general, the shock behavior of SC is relatively staightforward compared to B_4C and TiB_2. These two high strength ceramics exhibited heterogeneous deformations. The strain rate and pressure hardening behaviors in these ceramics did not resemble the metal behavior.

The pressure versus volumetric strain plot showed different loading and unloading paths. Since the model degraded the bulk modulus according to microcracking under tensile loading, the unloading path (see Figure 14) between the strains of 0.02 and zero differed from the loading path. The slight difference between the loading and unloading paths at strains above 0.04 was due to microcracking under compression. As mentioned earlier, the crack opening is possible under compressive pressure when one of the principal stresses is positive (tension).

The time histories of damage and axial stress at the midpoint of the ceramic target are plotted in Figure 15. To compare the stress with damage, the stress is normalized by the σ_{HEL} (= 15 GPa). The microcracking occurred at point "A" under compressive loading and reached a maximum of about 0.2 at point "B" in the figure. About t = 1.12 μs, the stress (see the dotted line) became tensile (negative in the figure) and damage reached one. In the model, the ceramic material at the midpoint of the target failed due to tensile cracking and could no longer support any tensile pressure.

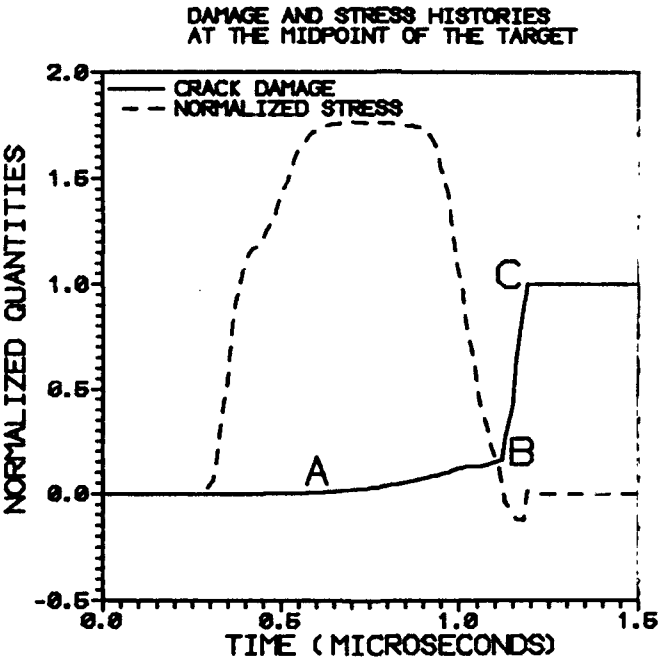

Figure 15. The computed damage and stress histories at a midsection of the SC target. The axial stress is normalized by σ_{HEL} = 15 GPa.

The maximum amplitude of the tensile stress is controlled by the degradation of shear and bulk moduli under tensile loading. When the crack density reaches a critical value of 9/16 in the Budiansky and O'Connell (19) relationship (see Appendix A), correspondingly the damage reaches one. At this time, both the moduli become zero. In the simulation, the element has failed under tension and can no longer transfer tensile pressure. The stresses and pressure are set to zero for the elements where the tensile damage reached the value of one at point "C". The elements are allowed to sustain compressive stresses until the element pulverizes under compressive crack growth.

Boron Carbide (B_4C)

Figure 16 compares the computed velocity profile with the experimental measurement for B_4C at 1546 m/s. Kipp and Grady (5) and Steinberg (6) provided some explanations for the unusual behavior of this material under high velocity impact loading. According to Kipp and Grady, the sporadic nature of the wave profile at the HEL is attributed in part to a heterogeneous failure or faulting mechanism during the initial shock loading. The plateau at the HEL also means a slower shock speed compared to the elastic wave speed. In the present study, an attempt is made to model the overall (or average) response of B_4C and, accordingly, the model constants were adjusted to reproduce the data in the best possible manner. The best constants for the ceramic model to describe the complex behavior of B_4C were obtained by matching the computed velocity histories with the data from test 3 (see Table 1). The corresponding comparison between the model and the data is given in Figure 16. The equation-of-state parameters and the model constants for B_4C were given earlier in Table 3 and Table 2, respectively. The measured velocity history in the high-stress amplitude, test 4 was predicted using the same set of constants.

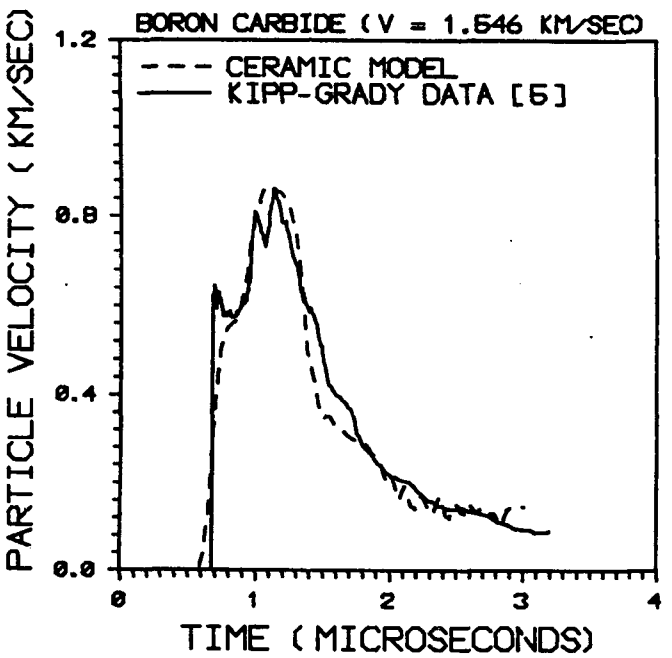

Figure 16. Comparison between model and Kipp and Grady (5) data for a boron carbide target (see test 3 in Table 1).

Figure 17 compares the computed velocity history with the measured data at 2210 m/s. The model matched the experimental data very well. The model could not capture the entire dispersive nature of the unloading portion of the velocity profile; however, the damage evolution through the time dependent microcracking process led to the degradation of elastic moduli and this degradation allowed some sort of dispersion of the unloading wave. In general, the ceramic model's ability to reproduce the data from the low and high velocity tests of B_4C is quite impressive.

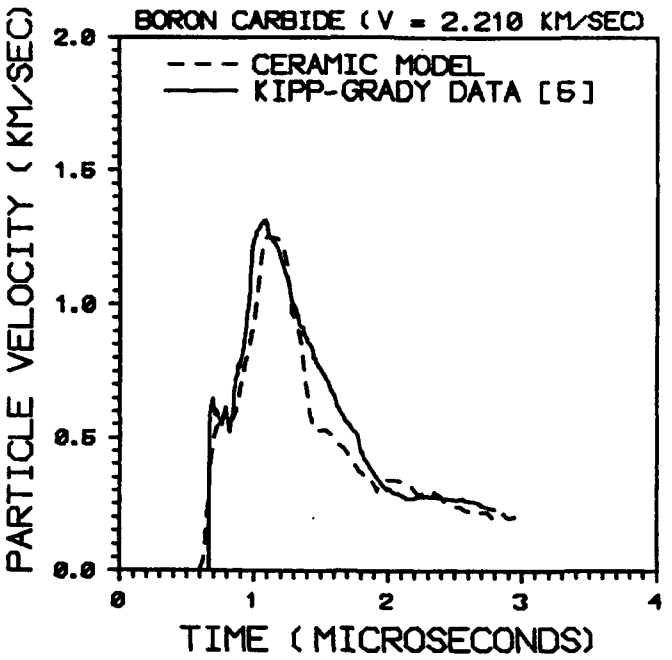

Figure 17. Comparison between model and Kipp and Grady (5) data for a boron carbide target (see test 3 in Table 1).

Titanium Diboride (TiB_2)

This material typically revealed two breaks in the loading wave portion of the measured profiles. In the present effort, no attempt is made to model the two breaks. The measured velocity histories from the two plate impact experiment; one at 1556 m/s and the other at 2075 m/s, are compared in Figure 18. The initial compressive loading in the lower velocity experiment (test 5) is very dispersive with a larger rise time compared to the higher velocity experiment (test 6). The release wave from the flyer arrives sooner in the higher velocity case. Since the flyer plate thickness in test 6 is smaller (3.337 mm) compared to the flyer plate in test 5 (3.972 mm), the pulse duration is shorter in test 6. In addition, the computational analysis of Kipp and Grady indicates shock wave formation above 13.7 GPa in TiB_2. This will also lead to a faster shock wave speed in the high velocity test compared to the dispersive loading wave in the lower velocity test and resulted in a shorter pulse duration.

The best suitable model constants were determined for TiB_2 by matching the computed velocity history with the data from test 5. These constants were given in Table 2. Figure 19 successfully compares the computed profile with the data. The ceramic model reproduced all the salient features of the measured velocity profile including the dispersive nature of the loading as well as the unloading waves. The high velocity test was predicted using the set of constants determined by matching the lower velocity test; the comparison is shown in Figure 20. The model showed more dispersion of the loading wave compared to the experiment. Assuming that TiB_2 shocks-up above a shock stress of about 32 GPa, the equation-of-state in conjunction with the constitutive equations was unable to model the high amplitude experimental data. However, a decent matching can be seen between the spall portions of the computed and experimental profiles.

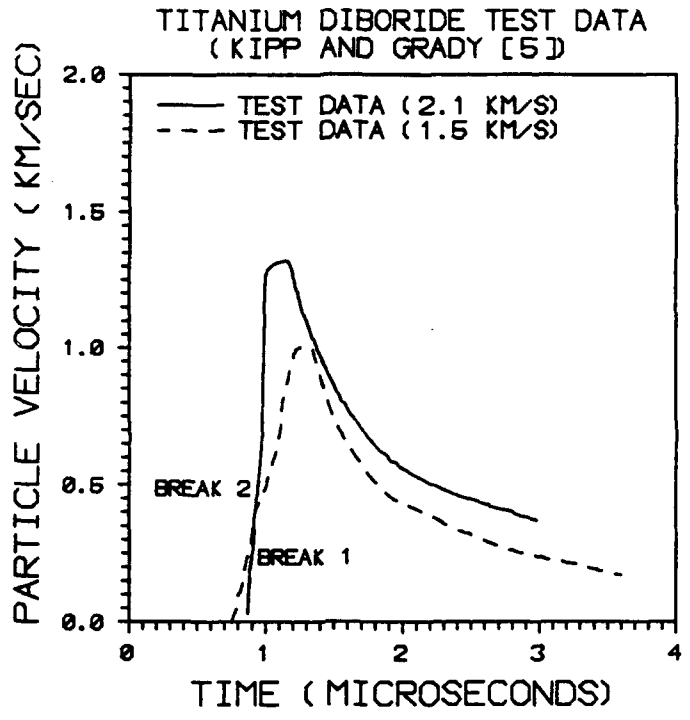

Figure 18. The measured velocity profiles from the two plate experiments of Kipp and Grady (5) on TiB_2 targets are compared.

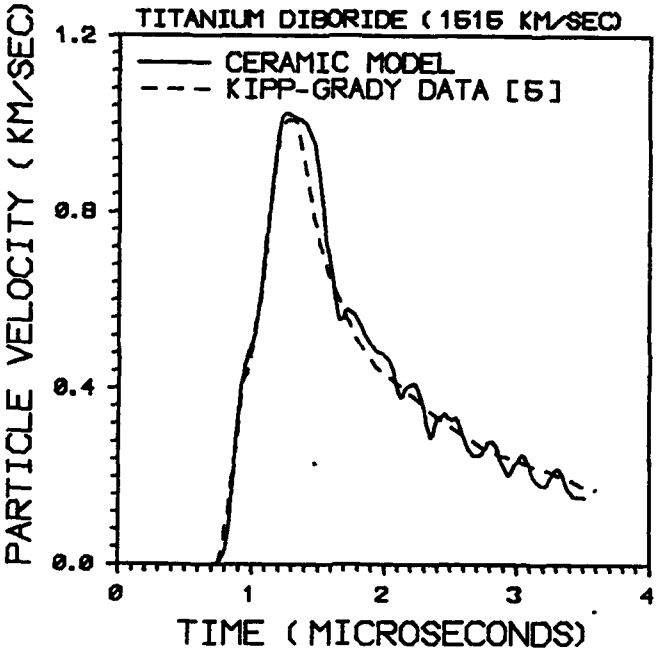

Figure 19. A comparison between model generated velocity profile with the Kipp and Grady plate impact experimental data at impact velocity of 1515 m/s for TiB_2.

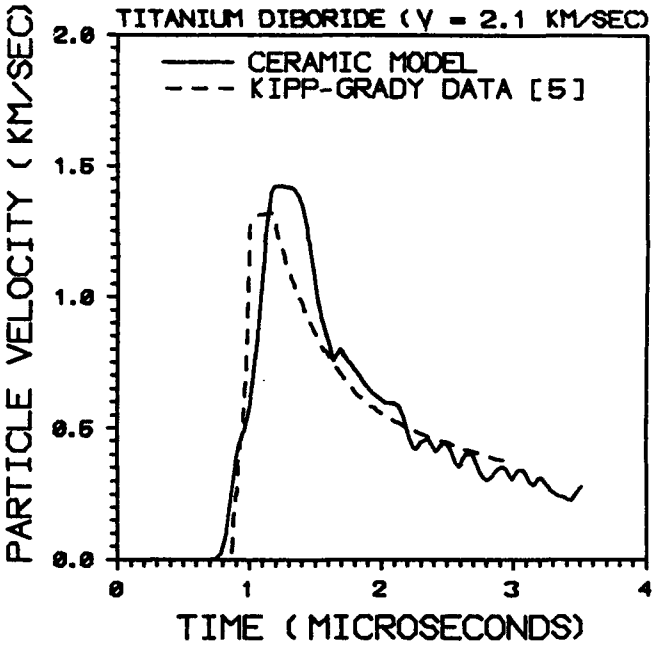

Figure 20. A comparison between model predicted velocity profile with the Kipp and Grady plate impact experimental data at impact velocity of 2100 m/s for TiB_2.

Summary and Conclusions

Summary

Recently, Rajendran (1,4) reported the development and application of an advanced ceramic model. This ceramic model has been implemented into the 1991 version of the EPIC-2 code by Grove (17) and successfully used to model the impact behavior of AD85 ceramic.

There are eight microcrack model constants: N_0^*, a_o, μ, K_{IC}, n_1^-, n_2^-, n_1^+, n_2^+. A porous ceramic requires one additional constant, f_o, which is the initial porosity. The fracture toughness value is taken from fracture mechanics handbooks. The coefficient of friction μ is assumed to be equal to 0.1 based on the sensitivity study. This value is arbitrarily assumed for SiC, B_4C, and TiB_2. The tensile crack growth factor, n_1^+, and the tensile crack growth index, n_2^+, are assumed to be equal to one; this eliminates the requirement for determining these two constants; therefore, the ceramic model effectively requires only four microcrack constants and one porosity constant.

The rest of the constants were calibrated by matching the simulated velocity or stress profiles with the measure profiles in a plate impact experiment. The strength model constants C_1 is assumed to be equal to the compressive strength value at HEL (Y_{HEL}). The rate sensitivity constants C_3 is calibrated by matching the shape of the elastic-plastic transition portion of the shock wave (velocity or stress) profile.

In summary, this report presented the impact behavior modeling of three ceramics: SC, B_4C, and TiB_2. The main objective of the present work was to determine the model constants for the model using the plate impact experimental measurements of Kipp and Grady (5). The following constants are assumed to be the same for all three ceramics:

$$\mu = 0.1,\ n_1^+ = 1.0,\ n_1^+ = 1.0,\ \text{and}\ n_2^- = 1.0\ . \qquad (12)$$

The other constants, a_o, N_0^*, n_{1-}, f_o, and C_3 were adjusted to give the best agreement with the data from the plate impact tests at 1.5 km/s.

Conclusions

In general, the inelastic deformation in ceramic materials due to impact loading, consists of elastic, plastic, and microcracking components. It is not experimentally possible to isolate these deformations through any direct measurements. With lack of any recovery techniques to examine the post-impacted ceramic targets, especially at high velocity impact, speculative assumptions can only be made on the various deformation and fracture processes.

The computational analysis of the impact experiments using advanced ceramic models will indeed help in evaluating the various possible deformation and fracture modes in the ceramic materials. So far the experimentalists have been making accurate velocity and stress measurements, high speed photographs, and X-ray radiographs. Interpretations and validations of these valuable measurements demand a detailed computational/analytical modeling of the impact experiments. These modeling efforts will eventually lead to a greater understanding of the impact behavior of ceramics.

In order to increase confidence in using the ceramic models as predictive tools in armor/anti-armor applications, generality of the model parameters should be tested using a variety of experimental data. The experiments should not only include various stress-strain states but also a range of velocity regimes. Though the high velocity (2.2 km/s) plate impact experiment could well be successfully predicted using the constants determined from the low velocity (2.5 km/s) one-dimensional experiment, the generality of the model constants required further validation.

For this purpose, other impact test configurations with different stress states should be modeled using the preliminary constants presented in this report. However, availability of a preliminary set of model constants for armor ceramics will encourage the scientists and engineers who perform advanced computational calculations in their design studies of armor/anti-armor to use advanced material constitutive and failure models.

In conclusion, this microphysical ceramic model is capable of modeling the impact behavior of the intact ceramic up to pulverization. Once the ceramic is pulverized, the accurate and realistic description of the confined pulverized ceramic requires improved equation-of-state and impact strength behavior models. In the computer code calculations, a simplistic Mohr-Coulomb type strength model (see Equation 11) is usually employed to describe the powdered ceramic. While the microphysical ceramic model is going to certainly improve the quality of computational armor/anti-armor design calculations, the absence of a microphysical model for the fractured (pulverized) ceramic unfortunately diminishes the ceramic model capability in predicting the depth of penetration/perforation of projectiles. Presently, Namat-Nasser and his students at the University of California in San Diego, CA, Clifton and his students at Brown University in Providence, RI, Curran and his coworkers at SRI International, and several other researchers are making progress towards the development of dilatational constitutive models for powdered ceramics.

Acknowledgments

The author gratefully acknowledges the support of Alan H. Katz and Colin Freese of the Mechanics of Materials Branch of Polymers and Mechanics Division in installing and compiling the EPIC-2 code on the Apollo Workstation. The author appreciates Dr. Shun-Chin Chou and Dr. Datta Dandekar of the Materials Dynamics Branch of Polymers and Mechanics Division for their critical reviews of the manuscript.

References

1. RAJENDRAN, A. M. *High Strain Rate Behavior of Metals, Ceramics, and Concrete.* Air Force Report, WL-TR92-4006, Wright-Patterson Air Force Base, OH 45433-6533, April 1992.
2. RAJENDRAN, A. M. *Modeling the Impact Behavior of AD85 Ceramic Under Multi-Axial Loading.* U.S. Army Research Laboratory, Report ARL-TR-137, May 1993.
3. GROVE, D. J., RAJENDRAN, A. M., BAR-ON, Eli., and BRAR, N. S. *Damage Evolution in a Ceramic Rod Shock Compression of Condensed Matter.* Elsevier Science Publishers, B.V., 1992, p. 971-974.
4. RAJENDRAN, A. M., and GROVE, D. J. *Modeling the Impact Behavior of AD85.* 24th Int. SAMPE Tech. Conf. Proceedings, Allied-Signal, Inc., Publishers, October 1992.
5. KIPP, M. E., and GRADY, D. E. *Shock Compression and Release in High-Strength Ceramics.* Sandia Report SAND89-1461, Sandia National Laboratory, NM 87185, July 1989.
6. STEINBERG, D. J. *Computer Studies of the Dynamic Strength of Ceramics.* Shock Compression of Condensed Matter. Elsevier Science Publishers, B.V., 1992, p. 447-450.
7. JOHNSON, G., and HOLMQUIST, T. J. *A Computational Constitutive Model for Brittle Materials Subjected to Large Strains, High Strain Rates, and High Pressures.* Shock Wave and High Strain Rates Phenomena in Materials, 1992.
8. ADDESSIO, F. L., and JOHNSON, J. N. *A Constitutive Model for the Dynamic Response of Brittle Materials.* LA-UR-89-2651, Los Alamos National Laboratory, Los Alamos, NM 87545.
9. MANDELL, D. A., and HENNINGER, R. *Evaluation of Two Ceramic Models in the Mesa Codes.* Los Alamos National Laboratory Report LA-12267, Los Alamos, NM 87545, February 1992.
10. HOLIAN, K. S., MOSSO, S. J., MANDELL, D. A., and HENNINGER, R. *A 3-D Computer Code for Armor/Anti-Armor Applications.* Los Alamos National Laboratory Report LA-UR-91-569, Los Alamos, NM 87545, 1991.
11. MARGOLIN, L. G. *Elastic Moduli of a Cracked Body.* Int. Journal of Fracture, v. 22, 1983, p. 65-79.
12. RAJENDRAN, A. M., DIETENBERGER, M. A., and GROVE, D. J. *A Void Growth-Based Failure Model to Describe Spallation.* J. Appl. Phys., v. 65, no. 4, 1989, p. 1521-1527.
13. JOHNSON, J. N. *Dynamic Fracture and Spallation in Ductile Solids.* J. Appl. Phys., v. 52, no. 4, 1981, p. 2812.
14. MARGOLIN, L. G. *A Generalized Griffith Criterion for Crack Propagation.* Engineering Fracture Mechanics, v. 19, v. 30, 1984, p. 539-543.
15. DIENES, J. K. Comments on *A Generalized Griffith Criterion for Crack Propagation* by L. G. Margolin. A Technical Note, Eng. Fracture Mechanics, v. 3, no. 23, 1986, p. 615-617.
16. KANNINEN, M. F., and POPELAR, C. H. *Advanced Fracture Mechanics.* Oxford University Press, New York, NY, 1985.
17. GROVE, D. J. Unpublished Works. University of Dayton Research Institute, Dayton, OH 45469, 1992.
18. JOHNSON, G. R., and STRYK, R. A. *User Instructions for the 1991 Version of the EPIC-2 Code.* Alliant Techsystems, Inc., Contract Report WL/MNW-TR-91-16, Brooklyn Park, MN, March 1991.
19. BUDIANSKY, B., and O'CONNELL, R. J. *Elastic Moduli of a Cracked Solid.* Int. J. of Solids and Structures, v. 12, 1976, p. 81-97.

Appendix

Degraded Moduli Expressions

The elastic stress-strain relationship in Equation 2 corresponds to the microcracked ceramic material. The elements of the stiffness matrix M in Equation 2 is obtained from the derivations of Margolin (11). Margolin derived the degraded elastic moduli for noninteracting, penny-shaped microcracks of various sizes and in random orientations. The components of the compliance (moduli) tensor C_{ijkl} which is the inverse of the stiffness tensor M_{ijkl} for the isotropic elastic moduli in Equation 3 is given by:

$$C_{ijkl} = C_1 \delta_{ik} \delta_{jl} + C_2 \delta_{il} \delta_{jk} + C_3 \delta_{ij} \delta_{kl} \tag{13}$$

where

$$C_1 = B_o + \frac{1}{4G} , \tag{14}$$

$$C_2 = D_o + \frac{1}{4G} , \tag{15}$$

and

$$C_3 = A_o - \frac{\nu}{2(1+\nu)G} . \tag{16}$$

In the above equations, G and ν are the shear modulus and Poisson's ratio, respectively, of the undamaged material while A_o, B_o, and D_o are damage parameters whose values depend on the stress state. To evaluate these parameters, Margolin defined a microcrack density parameter as

$$\gamma_0^* = \frac{16 N_0^* a_{max}^3}{45 E} . \tag{17}$$

In Equation 17, γ_0^* is the microcrack density and E is the Young's modulus of the undamaged material. N_0^* is the number of microcracks per unit volume, and a_{max} is the maximum microcrack size. Margolin identified the following four cases of stress state in evaluating the damage parameters A_o, B_o, and D_o:

Case 1:

$\overline{\sigma}_1, \overline{\sigma}_2, \overline{\sigma}_3 > 0$
(all prinicpal stresses are tensile)

$$A_o = \left[(1-\nu^2) - (1+\nu)\right]\gamma^* \tag{18}$$

$$B_o = \left[(1-\nu^2) + 4(1+\nu)\right]\gamma^* \tag{19}$$

$$D_o = A_o \tag{20}$$

Case 2:

$\overline{\sigma}_1, \overline{\sigma}_2, \overline{\sigma}_3 < 0$
(all principal stresses are compressive)

$$A_o = -(1+\nu)\gamma^* \tag{21}$$

$$B_o = 4(1+\nu)\gamma^* \tag{22}$$

$$D_o = A_o \tag{23}$$

Equations 21 through 23 will result in the degradation of the shear modulus but not of the bulk modulus because, under compression, only crack movement of the closed microcracks under modes II and III are permitted.

Case 3:

$\overline{\sigma}_1, \overline{\sigma}_2, > 0, \overline{\sigma}_3 < 0$
(two principal stesses are tensile and one principal stress is compressive)

$$A_o = \left[\frac{(5\beta^3 - 3\beta^5)}{2}(1-\nu^2) - (1+\nu)\right]\gamma^* \tag{24}$$

$$B_o = \left[\frac{(5\beta^3 - 3\beta^5)}{2}(1-\nu^2) + 4(1+\nu)\right]\gamma^* \tag{25}$$

$$D_o = \left[(6\beta^5 - 5\beta^3)(1-\nu^2) - (1+\nu)\right]\gamma^* \tag{26}$$

where

$$\beta \approx \sqrt{\frac{\overline{\sigma}_1 + \overline{\sigma}_2}{\overline{\sigma}_1 + \overline{\sigma}_2 - 2\overline{\sigma}_3}} \tag{27}$$

Case 4:

$\bar{\sigma}_1 > 0, \bar{\sigma}_2, \bar{\sigma}_3 < 0$

(one principal stress is tensile and two principal stresses are compressive)

$$A_o = \left[\frac{5(1-\beta^3) - 3(1-\beta^5)}{2} (1-\nu^2) - (1+\nu) \right] \gamma^* \tag{28}$$

$$B_o = \left[\frac{5(1-\beta^3) - 3(1-\beta^5)}{2} (1-\nu^2) + 4(1+\nu) \right] \gamma^* \tag{29}$$

$$D_o = \left\{ \left[6(1-\beta^5) - 5(1-\beta^3) \right] (1-\nu^2) - (1+\nu) \right\} \gamma^* \tag{30}$$

where

$$\beta \approx \sqrt{\frac{\bar{\sigma}_2 + \bar{\sigma}_3}{\bar{\sigma}_2 + \bar{\sigma}_3 - 2\bar{\sigma}_1}} \quad . \tag{31}$$

In the ceramic model, the compliance tensor C is analytically inverted to the stiffness tensor M using the following identity relationship:

$$M_{ijmn} C_{mnkl} = \frac{(\delta_{ik}\delta_{jl} + \delta_{il}\delta_{jk})}{2} \quad . \tag{32}$$

A relationship can be established between C_1, C_2, and C_3 of Equations 14 through 16 and m_1, m_2, and m_3 of the following relationship:

$$M_{ijkl} = m_1 \delta_{ik}\delta_{jl} + m_2 \delta_{il}\delta_{jk} + m_3 \delta_{ij}\delta_{kl} \tag{33}$$

where

$$m_1 = m_2 = \frac{1}{2(C_1 + C_2)} \tag{34}$$

and

$$m_3 = \frac{-C_3}{(C_1 + C_2)(C_1 + C_2 + 3C_3)} \quad . \tag{35}$$

The effective degraded shear and bulk moduli are defined as

$$\bar{G} = m \tag{36}$$

and

$$\bar{K} = m_3 + \frac{2}{3} m_1 \ . \tag{37}$$

Instead of employing Margolin's expression for Case 1 (all principal stresses are tensile), Budiansky and O'Connell (19) solutions can be used for randomly oriented, non-interacting microcracks under tensile loading. The corresponding relationships for the damaged stiffness solutions are:

$$m_1 = m_2 = \bar{G} \tag{38}$$

$$m_3 = \frac{2\bar{G}\ \bar{\nu}}{(1-2\bar{\nu})} \ , \tag{39}$$

where

$$\bar{\nu} = \nu \left(1 - \frac{16}{9} \gamma \right) , \tag{40}$$

and

$$\bar{G} = G \left\{ 1 - \left(\frac{32}{45} \right) \frac{(1-\bar{\nu})(5-\bar{\nu})}{(2-\bar{\nu})} \gamma \right\} \ . \tag{41}$$

In these equations, $\bar{\nu}$ and $\bar{G}$ are the Poisson's ratio and shear modulus, respectively, of the microcrack damaged material. Using m_1 and m_3 from Equations 38 and 39, the degraded bulk modulus can be computed from Equation 37. It is obvious from Equations 38 through 41 that a complete loss of strength is predicted when the microcrack density γ reaches 9/16. For tensile loading conditions, based on the comparison with Margolin's equations, there is no bound on the crack density; however, Budiansky and O'Connell's solution limits the crack density to 9/16. This permits the damage parameter to vary from zero (no damage) to one (fully damaged); therefore, in the ceramic model, Budiansky and O'Connell's equations are used instead of Margolin's equations for the case when all the principal stresses are positive (see Case 1).

DISTRIBUTION LIST

No. of Copies	To
1	Office of the Under Secretary of Defense for Research and Engineering, The Pentagon, Washington, DC 20301
	Director, U.S. Army Research Laboratory, 2800 Powder Mill Road, Adelphi, MD 20783-1197
1	ATTN: AMSRL-OP-SD-TP, Technical Publishing Branch
1	AMSRL-OP-SD-TM, Records Management Administrator
1	AMSRL-SS
	Commander, Defense Technical Information Center, Cameron Station, Building 5, 5010 Duke Street, Alexandria, VA 22304-6145
2	ATTN: DTIC-FDAC
1	MIA/CINDAS, Purdue University, 2595 Yeager Road, West Lafayette, IN 47905
	Commander, Army Research Office, P.O. Box 12211, Research Triangle Park, NC 27709-2211
1	ATTN: Information Processing Office
1	Dr. Andrew Crowson
1	Dr. Kailasam Iyer
	Commander, U.S. Army Materiel Command, 5001 Eisenhower Avenue, Alexandria, VA 22333
1	ATTN: AMCSCI
	Commander, U.S. Army Materiel Systems Analysis Activity, Aberdeen Proving Ground, MD 21005
1	ATTN: AMXSY-MP, H. Cohen
	Commander, U.S. Army Missile Command, Redstone Arsenal, AL 35809
1	ATTN: AMSMI-RD-CS-R/Doc
	Commander, U.S. Army Armament, Munitions and Chemical Command, Dover, NJ 07801
1	ATTN: Technical Library
	U.S. Army Communications and Electronics Command, Fort Monmouth, NJ 07703
1	ATTN: Technical Library
	Commander, U.S. Army Natick Research, Development and Engineering Center, Natick, MA 01760-5010
1	ATTN: Technical Library
	Commander, U.S. Army Satellite Communications Agency, Fort Monmouth, NJ 07703
1	ATTN: Technical Document Center
	Commander, U.S. Army Tank-Automotive Command, Warren, MI 48397-5000
1	ATTN: AMSTA-ZSK
1	AMSTA-TSL, Technical Library
1	AMSTA-RSK, Dr. James Thompson
	Commander, White Sands Missile Range, NM 88002
1	ATTN: STEWS-WS-VT

No. of Copies	To
	President, Airborne, Electronics and Special Warfare Board, Fort Bragg, NC 28307
1	ATTN: Library
	Director, U.S. Army Research Laboratory, Aberdeen Proving Ground, MD 21005-5066
1	ATTN: AMSRL-WT
1	AMSRL-WT-TA, George Hauver
1	AMSRL-WT-TD, Michael J. Scheidler
1	AMSRL-WT-TC, Kent Kinsey
1	AMSRL-WT-TD, Thomas W. Wright
1	AMSRL-WT-TD, Glenn Randers-Pehrson
1	AMSRL-WT-TD, Steven Segletes
1	AMSRL-TB-W
1	AMSRL-TB-AM
1	AMSRL-TB-P
1	AMSRL-AMB-TBD
1	William Gooch
	Commander, Dugway Proving Ground, UT 84022
1	ATTN: Technical Library, Technical Information Division
	Air Force Materials Directorate, WPAFB, OH 45433
1	ATTN: Dr. Theodore Nicholas
1	NASA - Langley Research Center, Hampton, VA 23665-5225
	U.S. Army Vehicle Propulsion Directorate, NASA Lewis Research Center, 2100 Brookpark Road, Cleveland, OH 44135-3191
1	ATTN: AMSRL-VP
	Director, Defense Intelligence Agency, Washington, DC 20340-6053
1	ATTN: ODT-5A (Mr. Frank Jaeger)
	Air Force Armament Laboratory, Eglin Air Force Base, FL 32542-5434
1	ATTN: Dr. J. C. Foster, Jr.
1	Dr. W. H. Cook
	Naval Post Graduate School, Monterey, CA 93943
1	ATTN: Dr. Joseph Sternberg, Code EW
	Lawrence Livermore, National Laboratory, Livermore, CA 94550
1	ATTN: J. E. Reaugh, L-290
1	R. L. Landingham, MC L-369
1	M. Finger, L-38
1	Daniel J. Steinberg
1	Carl R. Cline
	Naval Surface Warfare Center, Silver Spring, MD 20903-5000
1	ATTN: F. J. Zerilli, Code R13
1	R. H. Garrett, Jr.
	Naval Surface Warfare Center, Dahlgren, VA 22448
1	ATTN: William H. Holt, Naval Code G35

No. of Copies	To
	Los Alamos National Laboratory, Los Alamos, NM 87545
1	ATTN: Dr. R. Karpp, M-8, J960
1	Dr. J. Taylor, ADDRA, MS A11
1	Dr. J. N. Johnson, T-14, MS B214
1	Dr. P. J. Mauldlin, N-6, MS K557
1	Dr. F. Adessio, T-3, MS B216
1	Dr. Denise Hunter
1	Dr. Dave Mandell
1	Dr. B. M. Hogan
	Southwest Research Institute, 6220 Culebra Road, San Antonio, TX 78238
1	ATTN: Dr. James Lankford
1	Dr. C. E. Anderson
1	Dr. James Walker
	Southwest Research International, 333 Ravenswood Avenue, Menlo Park, CA 94025
1	ATTN: Dr. Richard Klopp
	Institute for Defense Analysis, 1801 N. Beauregard Street, Alexandria, VA 22311-1772
1	ATTN: Dr. George Mayer
1	Dr. Marc A. Adams, JPL MS 97-B, 4800 Oak Grove Drive, Pasadena, CA 91109
1	P.D. Buckley, NMIMT, TERA Group, Socorro, NM 87801
	California Institute of Technology, Geophysics Division MS/252-21, Pasadena, CA 91125
1	ATTN: Professor T. J. Ahrens
	Director, Benet Weapons Laboratory, LCWSL, USA AMCCOM, Watervliet, NY 12189
1	ATTN: AMSMC-LCB-TL
1	AMSMC-LCB-R
1	AMSMC-LCB-RM
1	AMSMC-LCB-RP
	Commander, U.S. Army Foreign Science and Technology Center, 220 7th Street, N. E., Charlottesville, VA 22901-5396
3	ATTN: AIFRTC, Applied Technologies Branch, Gerald Schlesinger
	Commander, U.S. Army Aeromedical Research Unit, P.O. Box 577, Fort Rucker, AL 36360
1	ATTN: Technical Library
	U.S. Army Aviation Training Library, Fort Rucker, AL 36360
1	ATTN: Building 5906-5907
	Commander, U.S.Army Agency for Aviation Safety, Fort Rucker, AL 36362
1	ATTN: Technical Library
	Commander, Clarke Engineer School Library, 3202 Nebraska Ave., N. Fort Leonard Wood, MO 65473-5000
1	ATTN: Library

No. of Copies	To
	Commander, U.S. Army Engineer Waterways Experiment Station, P.O. Box 631, Vicksburg, MS 39180
1	ATTN: Research Center Library
	Commandant, U.S. Army Quartermaster School, Fort Lee, VA 23801
1	ATTN: Quartermaster School Library
	Naval Research Laboratory, Washington, DC 20375
1	ATTN: Dr. G. R. Yoder - Code 6384
	Chief of Naval Research, Arlington, VA 22217
1	ATTN: Code 471
	Commander, U.S. Air Force Wright Research & Development Center, Wright-Patterson Air Force Base, OH 45433-6523
1	ATTN: WRDC/MLLP, M. Forney, Jr.
1	WRDC/MLBC, Mr. Stanley Schulman
	NASA - Marshall Space Flight Center, MSFC, AL 35812
1	ATTN: Mr. Paul Schuerer/EH01
	U.S. Department of Commerce, National Institute of Standards and Technology, Gaithersburg, MD 20899
1	ATTN: Stephen M. Hsu, Chief, Ceramics Division, Institute for Materials Science and Engineering
1	Committee on Marine Structures, Marine Board, National Research Council, 2101 Constitution Avenue, N. W., Washington, DC 20418
1	Materials Sciences Corporation, Suite 250, 500 Office Center Drive, Fort Washington, PA 19034
1	Charles Stark Draper Laboratory, 555 Technology Square, Cambridge, MA 02139
	Wyman-Gordan Company, Worcester, MA 01601
1	ATTN: Technical Library
	General Dynamics, Convair Aerospace Division, P.O. Box 748, Fort Worth, TX 76101
1	ATTN: Mfg. Engineering Technical Library
	Plastics Technical Evaluation Center, PLASTEC, ARDEC, Bldg. 355N, Picatinny Arsenal, NJ 07806-5000
1	ATTN: Harry Pebly
1	Department of the Army, Aerostructures Directorate, MS-266, U.S. Army Aviation R&T Activity - AVSCOM, Langley Research Center, Hampton, VA 23665-5225
	Department of the Army, Armament Research and Development Center, Dover, NJ 07801
1	ATTN: Dr. E. Bloore

No. of Copies	To
1	Department of the Army, Aerostructures Directorate, MS-266, U.S. Army Aviation R&T Activity - AVSCOM, Langley Research Center, Hampton, VA 23665-5225
	GTE Products Corporation, Towanda, PA 18848
1	ATTN: Jeff Gonzalez
	RARDE, Fort Halstead - Sevenoaks, TN14 7BP Kent, England
1	ATTN: Dr. Phillip Church
	Department of FV&S7, DRA (Chertsey), Chobham Lane, Chertsey, Surrey, England
1	ATTN: Dr. Anthony Hawkins
	National Defense Research Establishment, Box 27322, S-102 54 Stockholm, Sweden
1	ATTN: Dr. Per-Olof Olsson
	Brown University, Division of Engineering, 182 Hope Street, Providence, RI 02912
1	ATTN: Prof. Clifton
	California Research & Technology, Inc., 5117 Johnson Drive, Pleasanton, CA 94566
1	ATTN: Dennis L. Orphal
	The Carborundum Company, P.O. Box 1054, Niagra Falls, NY 19302
1	ATTN: Robert Palia
	Institute for Advanced Technology, 4030-2 West Braker, Austin, TX 78759-5329
1	ATTN: Dr. Stephen Bless
	University of Dayton Research Institute, KLA14, 300 College Park, Dayton, OH 45469-0182
1	ATTN: Dr. N. Singh Brar
	University of Dayton, Building JPC 201, Dayton, OH 45469
1	ATTN: Mr. David J. Grove
	General Dynamics, Land Systems Division, P.O. Box 1800, Warren, MI 48090
1	ATTN: Wayne A. Burke
	General Research Corporation, 5383 Hollister Avenue, Santa Barbara, CA 93160-6770
1	ATTN: Alex Charters
1	T. L. Menna
	Sandia National Laboratories, P.O. Box 5800, Albuquerque, NM 87185
1	ATTN: Peter Chen
1	Dr. Dennis E. Grady, ORG 1533
1	Dr. Jack L. Wise
	The Pentagon, ODDR&E, Washington, DC 20305
1	ATTN: Dr. W. E. Snowden
	DARPA/Materials Science Office, 1400 Wilson Boulevard, Arlington, VA 22209-2308
1	ATTN: Dr. B. Wilcox

No. of Copies	To
	Trans Science Corporation, P.O. Box 2727, La Jolla, CA 92038
1	ATTN: Dr. G. A. Hegemier
	Purdue University, School of Aeronautics & Astronautics, West Lafayette, IN 47907
1	ATTN: Dr. Horacio D. Espinosa
	University of California - San Diego, Department of Applied Mechanics & Engineering Services - R011, La Jolla, CA 92093-0411
1	ATTN: Prof. Sia Nemat-Nasser
	DARPA/TTO, 3701 North Fairfax Drive, Arlington, VA 22203-1714
1	ATTN: Robert Kocher
	Lanxide Armor Products, Inc., 1300 Marrows Road, P.O. Box 6077, Newark, DE 19714-6077
1	ATTN: Katherine T. Leighton
	University of Hawaii at Monoa, Mineral Physics Group, Department of Geology & Geophysics 255 Correa Road, Honolulu, HI 96822
1	ATTN: Prof. Murli Manghnani
	Kaman Sciences Corporation, P.O. Box 7463, 1500 Garden of the Gods Road, Colorado Springs, CO 80933
1	ATTN: Dr. Michael J. Normandia
	Cercom, 1950 Watson Way, Vista, CA 92083
1	ATTN: Dr. Rich Palicka
	Poulter Laboratory, SRI International, 333 Ravenswood Avenue, Menlo Park, CA 94025
1	ATTN: Dr. Donald Curran
1	Dr. Lynn Seaman
1	Dr. Donald A. Shockey
1	Dr. Robert D. Caligiuri
	Alliant Techsystems, Inc., 7225 Northland Drive, Brooklyn Park, MN 55428-1515
1	ATTN: T. J. Holmquist
1	Dr. Gordon R. Johnson
	E. I. Du Pont de Nemous & Company, Wilmington, DE 19898
1	ATTN: Dr. Barry E. Bowen
	California Research & Technology, Inc., 5771 Johnson Drive, Pleasanton, CA 94566
1	ATTN: Dr. Ronald E. Brown
	Aeronautical Research Associates of Princeton, Inc., 50 Washington Road, P.O. Box 2229, Princeton, NJ 08540
1	ATTN: Dr. Ross M. Contiliano
	Dow Chemical Company, Midland, MI 48640
1	ATTN: Mr. Kenneth O. Groves
	Director, U.S. Army Research Laboratory, Watertown, MA 02172-0001
2	ATTN: AMSRL-OP-WT-IS, Technical Library
5	Author